Atomic Spectroscopy

Article

Doppler-shift Measurement of Pressure-dependent Expansion Velocities in Laser-ablated Molybdenum Plasma

Xiaohan Hu, Ding Wu,[a,*] Xinyue Wang,[a] Haobo Heng,[a] Ke Xu,[a] Huace Wu,[b] Ran Hai,[a] Cong Li,[a] Chunlei Feng,[a] and Hongbin Ding [a,*]

[a] Key Laboratory of Materials Modification by Laser, Ion and Electron Beams, Chinese Ministry of Education, School of Physics, Dalian University of Technology, Dalian 116024, P. R. China

[b] Institute of Energy, Hefei Comprehensive National Science Center (Anhui Energy Laboratory), Hefei 230031, P. R. China

Received: *July 01, 2026;* ***Revised:*** *September 13, 2026;* ***Accepted:*** *September 26, 2026;* ***Available online:*** *September 26, 2026.*

DOI: 10.46770/AS.2026.0050s

ABSTRACT: Molybdenum (Mo) is used as a first-wall material in EAST, where laser-induced breakdown spectroscopy (LIBS) is a promising tool for *in-situ* diagnostics of plasma-wall interactions (PWIs). The large variation in ambient pressure during EAST operation can significantly affect the expansion of laser-ablated plasmas and, consequently, the stability of LIBS signals. In this study, plasma emission spectra were recorded in coaxial and orthogonal detection geometries using a high-resolution Echelle spectrometer, and the differential Doppler shifts between the two geometries were used to investigate the pressure-dependent normal expansion velocities of Mo atoms and ions over an ambient pressure range of 4×10^{-5}-6×10^{2} mbar. At low pressures (4×10^{-5}-3×10^{-2} mbar), Mo atoms and ions maintained relatively high expansion velocities with weak pressure dependence, reaching approximately 4-6 km/s and 11-15 km/s, respectively. Local maxima in the velocities of both species were observed near 10^{-1} mbar. At pressures above 1 mbar, the velocities decreased rapidly owing to enhanced collisions and confinement by the background gas. The pressure-dependent trends obtained using the Doppler-shift method agreed well with those determined by time- and space-resolved spectroscopy. These results demonstrate the applicability of Doppler-shift spectroscopy for non-contact velocity diagnostics of laser-ablated Mo plasma and provide experimental guidance for interpreting and optimizing LIBS measurements under EAST-relevant pressure conditions.

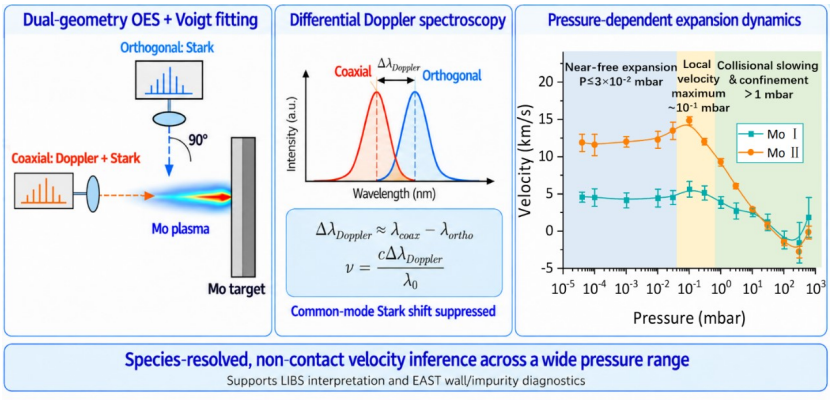

INTRODUCTION

During the operation of tokamak devices, plasma-wall interactions (PWIs) are inevitable. These interactions can lead to microstructural degradation of plasma-facing materials (PFMs) and increased fuel retention. In severe cases, they may also cause impurity-induced radiative cooling and plasma dilution, thereby significantly degrading plasma confinement and stability[1-5]. Molybdenum (Mo), owing to its high melting point, low sputtering yield, low fuel retention and relatively low cost, has been employed as a first-wall material in EAST[6-9]. To gain deeper insight into the processes and mechanisms of PWIs, continuous elemental diagnostics and condition monitoring of PFMs are crucial[10-12]. Accordingly, systematic characterization of Mo materials and the evolution of their erosion, migration and deposition processes is necessary[13, 14].

Laser-induced breakdown spectroscopy (LIBS), owing to its capabilities for *in-situ* analysis, no sample preparation and rapid

multi-element detection, is regarded as a promising technique for condition monitoring and fuel/impurity diagnostics of PFMs in tokamak devices[15-18]. The LIBS response depends on many parameters, including laser parameters (irradiance, pulse duration, fluence, and wavelength), sample characteristics (optical absorption coefficient, surface reflectivity, thermal diffusivity, thermal conductivity, and melting and boiling points), ambient gas conditions, and the amount of ablated material[19-21]. Among these factors, ambient pressure plays an important role because it strongly influences the transient spatiotemporal evolution of the laser-ablated plasma plume, thereby affecting the continuum background, spectral-line intensities, and line-shape parameters[22, 23]. During EAST operation, the vacuum chamber pressure spans several orders of magnitude depending on the operational stage[24-26]. For example, after pump-down and wall conditioning, the pressure can be reduced to approximately 10^{-8} mbar. Glow discharge cleaning (GDC) is typically performed in the range of 5×10^{-3}-10^{-1} mbar, while ion cyclotron radio frequency discharge cleaning (ICRF-DC) is usually carried out at around 10^{-5} mbar, depending on the operational cycle and conditions. During maintenance shutdown periods, the chamber is filled with pure nitrogen or air to a pressure of 10^{3} mbar. Over such a wide pressure range, the propagation characteristics and plasma parameters of laser-ablated plasma plumes change markedly. These variations affect the optimization of LIBS acquisition parameters (e.g., gate delay and integration time), as well as the consistency of LIBS calibration and the accuracy of quantitative analysis[27-29]. Therefore, understanding pressure-dependent plume dynamics is essential for both elucidating the fundamental processes governing laser-ablated plasma and developing reliable quantitative spectroscopic models for LIBS. As a practical and informative descriptor of plume dynamics, the expansion velocity provides direct insight into the evolution of the Mo plasma plumes and their dependence on ambient pressure, thereby improving the controllability, repeatability, and comparability of LIBS diagnostics. Such information may also facilitate *in-situ* diagnostics of Mo-related impurity behavior in EAST.

In experimental studies, the expansion velocity of laser-ablated plasma plumes is commonly determined using two approaches. The first is gated ICCD fast imaging, in which the plume front or the position of the maximum emission intensity is identified at different delay times to determine the expansion velocity. The second is time- and space-resolved emission spectroscopy, in which the arrival time of the peak intensity of a characteristic spectral line is recorded at different spatial positions, allowing the expansion velocity to be determined. For example, Whitty et al.[30] estimated the expansion velocities of lithium plasma plumes in vacuum and in argon at a pressure of 200 mTorr using gated ICCD imaging; Camacho et al.[31] obtained the velocity distributions of N^+ and O^+ emission lines at atmospheric pressure using time-resolved spectroscopy; Irimiciuc et al.[32] combined ICCD imaging with time- and space-resolved optical emission spectroscopy to reveal the plume dynamics and angular distributions of plume front velocities for laser-ablated Al and Ag-Ni-Fe plasmas at 10^{-2} Torr. Dawood et al.[33] investigated laser-ablated aluminum plasmas in different ambient gases (He, N_2, or Ar) over a range of pressures, determined the plume expansion velocities using both ICCD imaging and time- and space-resolved emission spectroscopy, and compared the results to clarify the mechanisms responsible for the observed differences.

Although gated imaging and time- and space-resolved spectroscopy can be used to determine plume expansion velocities, Doppler-shift spectroscopy provides a complementary diagnostic approach. These conventional methods primarily characterize the apparent propagation of the plume front or the position of maximum emission intensity, whereas the Doppler-shift method directly measures the line-of-sight velocity component of a specific emitting species. However, systematic measurements of the pressure-dependent, species-resolved expansion velocities of laser-ablated Mo plasma over a broad pressure range remain limited. Therefore, the aim of this study is to investigate the pressure-dependent normal expansion velocities of Mo atoms and ions using differential Doppler-shift measurements and to evaluate the applicability of this approach over 4×10^{-5}-6×10^{2} mbar. In this work, optical emission spectroscopy was employed to acquire the emission spectra of laser-ablated Mo plasma under different ambient pressures. Representative Mo atomic and ionic spectral lines were selected, and their peak wavelength shifts were analyzed to retrieve the corresponding velocities based on the Doppler effect. The novelty of this study lies in the use of coaxial and orthogonal detection geometries to suppress common spectral-shift contributions and estimate the dominant Doppler-related component, enabling the normal expansion velocities of Mo atoms and ions to be systematically characterized over 4×10^{-5}-6×10^{2} mbar. The Doppler-derived velocities were further compared with those obtained using time- and space-resolved spectroscopy, providing complementary validation of the observed pressure-dependent trends. This approach provides species-resolved information on plume expansion and helps clarify the pressure-dependent mechanisms governing energy and mass transport in laser-ablated Mo plasma under conditions relevant to EAST-oriented LIBS diagnostics.

EXPERIMENTAL

The schematic diagram of the experimental setup is shown in Fig. 1. A nanosecond Q-switched Nd:YAG laser (Brilliant Eazy, Quantel), with a pulse duration of 5 ns and a repetition rate of 2 Hz, was operated at the fundamental wavelength of 1064 nm to generate the plasma. Considering its application as a first-wall material in EAST, molybdenum was selected as the target material in this study. A high-purity Mo sample (>99.95%) was used to minimize

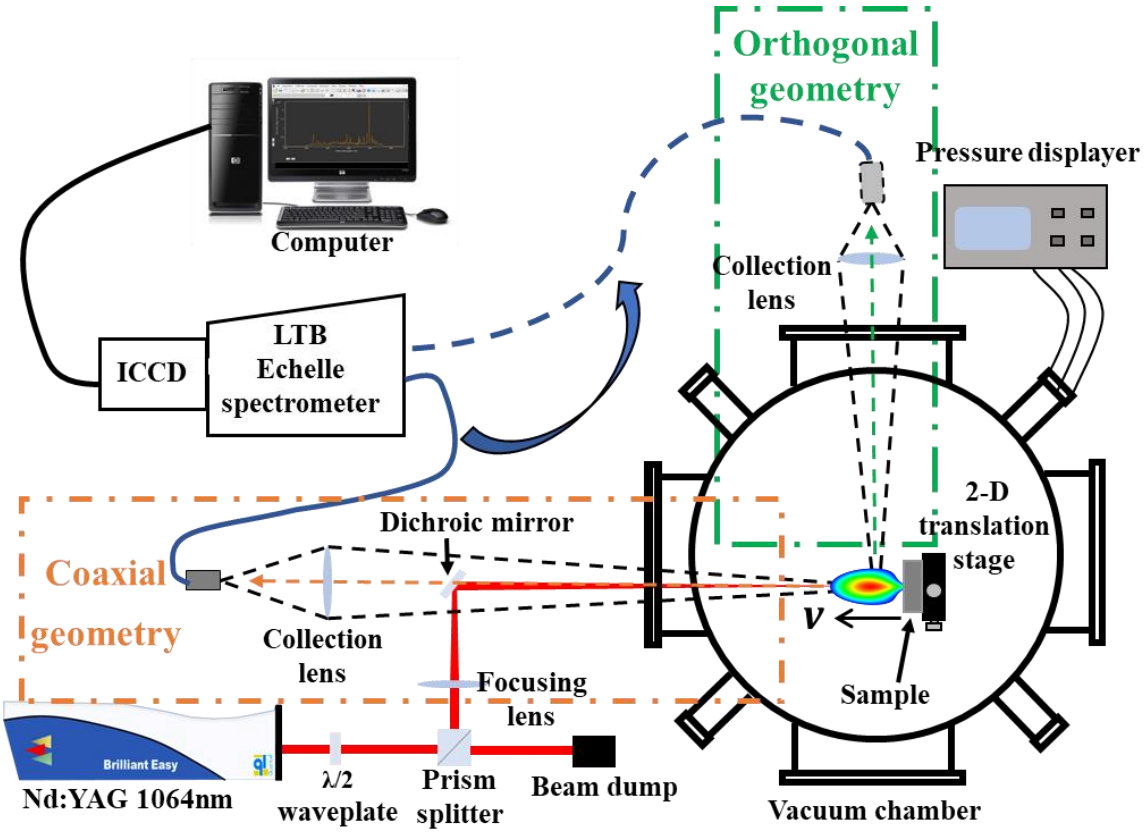

Fig. 1 Schematic diagram of the LIBS experimental setup.

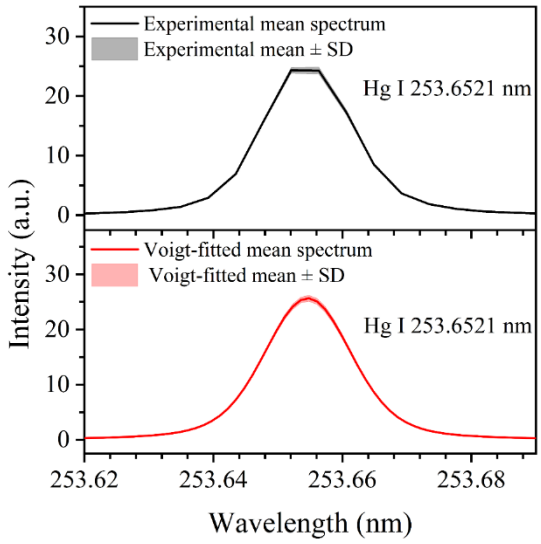

Fig. 2 Hg I 253.6521 nm emission line from the argon-mercury lamp: (a) mean spectrum and standard deviation obtained from ten repeated measurements; (b) Voigt-fitted mean spectrum with its associated uncertainty.

spectral interference from impurity elements. The laser beam was focused vertically onto the surface of the Mo sample by a plano-convex lens with a focal length of 500 mm. The Mo sample was mounted on a two-dimensional motorized translation stage inside the vacuum chamber, allowing the ablation position to be conveniently adjusted. The laser pulse energy after focusing and transmission through the quartz window of the vacuum chamber was 150 mJ, measured by a laser power meter (842-PE, Newport). The laser spot diameter, determined by scanning the ablation crater with a confocal microscope (Micromeasure2, France), was approximately 0.8 mm, corresponding to the laser power density of 6.0 GW/cm². The experiments were conducted in a vacuum chamber filled with air as the background gas, with pressures varying from 4×10^{-5} mbar to 10^{3} mbar.

Optical emission from the laser-ablated Mo plasma was collected using a plano-convex lens with a focal length of 100 mm in two detection geometries: one with the collection axis parallel to the laser-beam propagation direction and the other with the collection axis perpendicular to it. Apart from the detection configuration, all experimental conditions were kept identical. The collected plasma emission was coupled into an optical fiber bundle with a core diameter of 1 mm and connected to an Echelle spectrograph (ARYELLE Butterfly, LTB) equipped with an ICCD (iStar DH334T, Andor). The ratio of the object distance to the image distance of the collection lens was approximately 6,

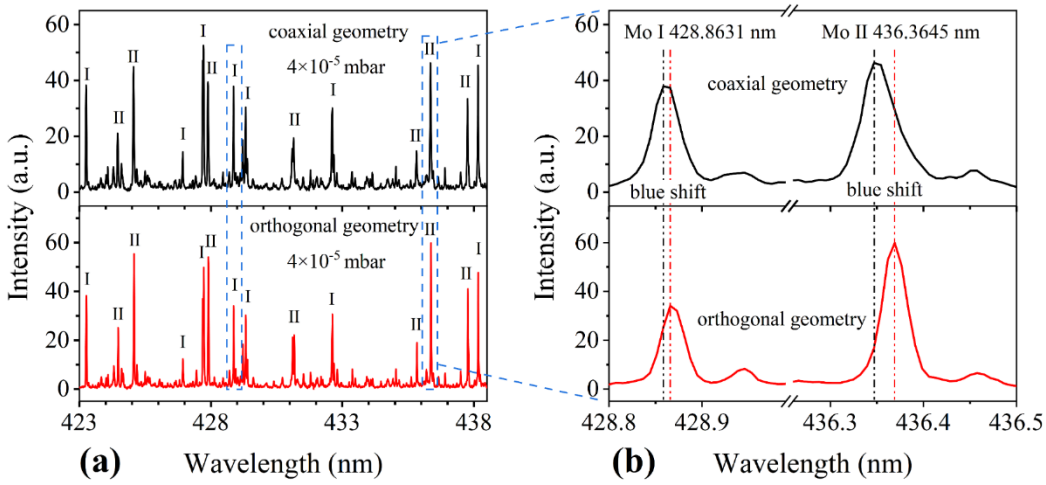

Fig. 3 Emission spectra of Mo plasma collected in coaxial and orthogonal detection geometries at 4×10^{-5} mbar: (a) the spectral wavelength range from 423.0 to 438.5 nm; (b) enlarged views of the selected Mo I 428.8631 nm and Mo II 436.3645 nm lines.

corresponding to a plasma collection region of about 6 mm. The measured spectral range was 192-440 nm, with the spectral resolution $\lambda/\Delta\lambda$ of 25000. To obtain spectra with adequate signal quality over the investigated pressure range, the spectrometer gate delay time was set to t_d = 200 ns, and the gate width was set to t_w = 1 μs. To minimize the influence of surface contaminants and roughness on the experimental results, the sample was pre-cleaned with 10 laser pulses at each new ablation point before data acquisition.

The Doppler-shift measurement is based on the different line-of-sight velocity components sampled by the two detection geometries. Because the laser-ablated plasma expands predominantly along the target surface normal, the coaxial geometry detects a substantial velocity component along the line of sight and therefore exhibits a pronounced Doppler shift. In contrast, the orthogonal geometry is approximately perpendicular to the dominant expansion direction, and the corresponding Doppler contribution is strongly suppressed. Therefore, the wavelength difference between the coaxial and orthogonal geometries can be used to determine the Doppler-induced shift associated with the normal expansion of the plasma. The corresponding expansion velocity is then derived from the classical Doppler relation. Other contributions to the wavelength shift, particularly the Stark shift, are discussed in detail in the Section of "Pressure dependence of peak wavelength shifts in coaxial and orthogonal geometries".

The wavelength measurement stability of the spectrometer was evaluated using the Hg I emission line at 253.6521 nm from an argon-mercury lamp. Ten consecutive spectra were recorded under identical conditions, and the mean spectrum and corresponding standard deviation were calculated, as shown in Fig. 2(a). The measured line profile was further fitted with a Voigt function to accurately determine the line-center wavelength, as shown in Fig. 2(b). The slight differences among repeated measurements confirmed the wavelength stability and repeatability of the spectrometer, ensuring the reliability of subsequent Doppler-shift measurements. The standard deviation of the peak wavelength obtained from ten Voigt fittings of Hg I 253.6521 nm was 3.29×10^{-5} nm, which is two to three orders of magnitude smaller than the Doppler shifts of the Mo spectral lines discussed below and can therefore be considered negligible.

RESULTS AND DISCUSSION

Optical emission spectra in coaxial and orthogonal detection geometries. Fig. 3(a) shows the emission spectra of laser-ablated Mo plasma collected in coaxial and orthogonal detection geometries in the wavelength range of 423.0-438.5 nm at 4×10^{-5} mbar. The Roman numerals I and II denote spectral lines from atomic Mo (Mo I) and ionic Mo (Mo II), respectively. For subsequent analysis, eight representative spectral lines with relatively high intensities and good spectral isolation were selected. The corresponding spectroscopic parameters are summarized in Table 1, where A_{ki} is the transition probability, E_i and E_k are the lower and upper energy levels of the transition, respectively, and g_k is the statistical weight of the upper level. These parameters were obtained from the Kurucz database[34]. As shown in the enlarged spectra in Fig.3 (b), the Mo I 428.8631 nm and Mo II 436.3645 nm lines acquired in the coaxial geometry exhibit clear shifts toward shorter wavelengths (blue shifts) compared with those recorded in the orthogonal geometry, consistent with shifts induced by the Doppler effect.

Table 1. Selected Mo I and Mo II emission lines and their associated parameters obtained from the Kurucz database[34]

Species	Wavelength in database (nm)	A_{ki} (s^{-1})	E_i (eV)	E_k (eV)	g_k
Mo I	423.2589	3.16×10^7	2.08	5.00	11
Mo I	426.9279	1.36×10^7	2.65	5.55	11
Mo I	428.8631	1.05×10^7	1.47	4.36	9
Mo I	438.163	2.93×10^7	2.08	4.91	13
Mo II	424.4747	9.20×10^6	4.50	7.42	4
Mo II	427.9022	9.10×10^6	3.06	5.95	4
Mo II	436.3645	9.70×10^6	3.11	5.95	4
Mo II	437.7775	1.40×10^7	3.02	5.85	2

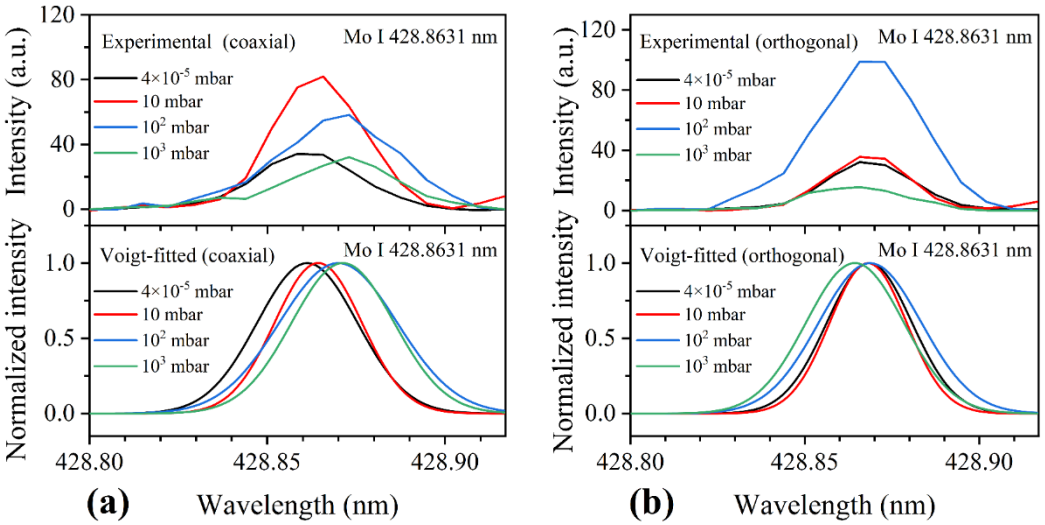

Fig. 4 Mo I 428.8631 nm spectral line profiles acquired at different ambient pressures:(a) spectra obtained in the coaxial geometry and the corresponding normalized Voigt-fitted profiles;(b) spectra obtained in the orthogonal geometry and the corresponding normalized Voigt-fitted profiles.

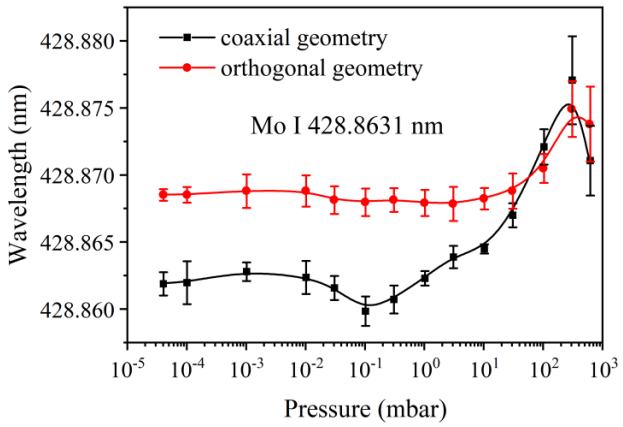

Fig. 5 Pressure dependence of the Voigt-fitted peak wavelength of the Mo I 428.8631 nm spectral line measured in coaxial and orthogonal detection geometries.

Pressure dependence of peak wavelength shifts in coaxial and orthogonal geometries. Fig. 4 presents the experimental line profiles of Mo I 428.8631 nm acquired in coaxial and orthogonal geometries at different ambient pressures, together with the corresponding Voigt-fitted profiles. The experimental spectra show that increasing the ambient pressure from 4×10^{-5} to 10^3 mbar produces pronounced changes in both line intensity and profile shape. At low pressures, the emission line is narrow; as the pressure increases, it progressively broadens. To characterize the pressure-dependent variation in peak wavelength more quantitatively, the experimental spectra were fitted using a Voigt function, and the fitted profiles were subsequently normalized. The normalized Voigt-fitted profiles obtained in the coaxial geometry show evident pressure-dependent shifts in peak wavelength, indicating that the peak position is highly sensitive to ambient pressure. In comparison, the variation in peak wavelength with pressure is substantially weaker in the orthogonal geometry. Voigt fitting reduces the influence of experimental noise on peak wavelength determination, enabling clearer identification of the pressure-dependent trend and providing a reliable basis for the subsequent analysis of peak wavelength shifts. It should be noted that at 10^3 mbar (atmospheric pressure), the line broadening and line shape distortion are significantly enhanced due to strong coupling between the plasma plume and the background gas, leading to increased fitting uncertainty. Therefore, to avoid additional bias, the peak wavelength shift and the corresponding velocity inferred from it at this pressure were not further analyzed in this work.

The evolution of the peak wavelength of the Mo I 428.8631 nm spectral line as a function of ambient pressure is compared between the coaxial and orthogonal detection geometries in Fig. 5. In the coaxial geometry, the peak wavelength remains nearly unchanged in the low-pressure regime from 4×10^{-5} to 3×10^{-2} mbar, with a local minimum observed around 10^{-1} mbar. When the ambient pressure exceeds 1 mbar, the peak wavelength shifts noticeably toward longer wavelengths compared with that observed at lower pressures. In contrast, the peak wavelength measured in the orthogonal geometry remains almost stable over a wider pressure range from 4×10^{-5} to 10 mbar, with no obvious systematic drift. The noticeable shift appears only in the high-pressure regime above 10^2 mbar, and its magnitude is much smaller than that observed in the coaxial geometry.

These geometry-dependent differences indicate that the measured peak wavelength shift cannot be attributed to a single mechanism. Instead, it is mainly determined by the combined contributions of the Doppler shift and the Stark shift, while the van der Waals shift caused by collisions with neutral species is estimated to be less than 1 pm over the pressure range investigated here[35] and is therefore neglected in the following discussion. Accordingly, the observed wavelength shift of the spectral line can be approximately expressed as:

$$\Delta\lambda_{obs}(p) = \Delta\lambda_D(p) + \Delta\lambda_{Stark}(p) \qquad (1)$$

Where $\Delta\lambda_{obs}(p)$ is the observed wavelength shift at a given pressure, and $\Delta\lambda_D(p)$ and $\Delta\lambda_{Stark}(p)$ represent the Doppler and Stark contributions, respectively.

For laser-ablated plasma plumes, the expansion is highly anisotropic, with the largest expansion velocity generally occurring along the direction normal to the target surface[27]. In the non-relativistic limit $v \ll c$, the classical Doppler relation can be expressed as[36]:

$$f' = f\left(1 + \frac{v}{c}cos\alpha\right) \qquad (2)$$

Where f' is the observed frequency, f is the intrinsic frequency of the radiator, v is the velocity of the emitting species relative to the observer, c is the speed of light, and α is the angle between the velocity vector and the line-of-sight direction. Therefore, changing the observation direction alters the line-of-sight component of the emitter's velocity, leading to a pronounced variation in the Doppler contribution to the measured wavelength shift.

In the coaxial detection geometry, the spectral collection direction is approximately aligned with the dominant expansion direction of the plasma plume. Therefore, the velocity component projected along the coaxial observation direction, $v_{\parallel}$, is relatively large, making the measured peak wavelength highly sensitive to the plume expansion dynamics. With increasing pressure, enhanced plume-background gas collisions lead to pronounced deceleration, compression and the development of shock-wave structures [37, 38], thereby substantially modifying the axial velocity field and the spatial distribution of the emitting region. Because the experimentally observed $v_{\parallel}$ essentially represents a radiation-weighted projection of the velocity distribution within the emitting region, this reconfiguration can substantially modify its weighted mean value. Consequently, these effects produce a pronounced pressure dependence of the spectral line peak wavelength in the coaxial detection geometry.

In the orthogonal detection geometry, the spectral collection direction is approximately perpendicular to the dominant expansion direction of the plasma plume. As a result, the projection of the particle velocity onto this observation axis, $v_{\perp}$, is much smaller. In addition, the volume-integrated emission collected by the orthogonal optical system contains nearly symmetric red- and blue-shifted contributions from opposite velocity components, which tend to cancel each other. Therefore, the net Doppler shift is strongly suppressed in the orthogonal geometry, explaining why the peak wavelength remains much less sensitive to pressure than the wavelength measured in the coaxial geometry.

In addition to the Doppler effect, the Stark effect can also shift spectral line due to the micro-electric fields generated by electrons and ions in the plasma. The Stark shift depends mainly on the electron density n_e, with a weaker dependence on the electron temperature T_e[35]. Fig. 6 presents the pressure dependence of n_e and T_e obtained in coaxial and orthogonal detection geometries. The n_e and T_e were calculated using the spectral matching algorithm based on Saha-Boltzmann equilibrium, and the detailed procedure can be found in our previous work[39]. As shown in Fig. 6(a), the n_e values measured in the two geometries exhibit a similar pressure-dependent trend. In the low-pressure regime from 4×10^{-5} to 10^{-1} mbar, n_e remains relatively low and nearly stable in both geometries, with values in the range of $(3.0\text{-}4.0)\times10^{22}$ m^{-3}. When the pressure increases above 1 mbar, n_e begins to increase rapidly, reaching $(1.5\text{-}1.7)\times10^{24}$ m^{-3} in both geometries at $(3\text{-}6)\times10^2$ mbar. Similarly, Fig. 6(b) shows that the T_e values obtained in the two geometries are also in good agreement over most of the investigated pressure range. The T_e values obtained in the two detection geometries remain nearly unchanged from 4×10^{-5} to 10^{-1} mbar, with both lying in the range of 0.83-0.87 eV. T_e then gradually increases with pressure. At $(3\text{-}6)\times10^2$ mbar, T_e remains in the range of 1.33-1.42 eV for both detection geometries. However, in the pressure range of 10-10^2 mbar, the n_e values obtained in the two geometries exhibit certain deviations, which may be attributed to the strong spatial redistribution of the plasma plume in this transition-pressure regime, in which different detection geometries sample different emission-weighted regions of the plasma.

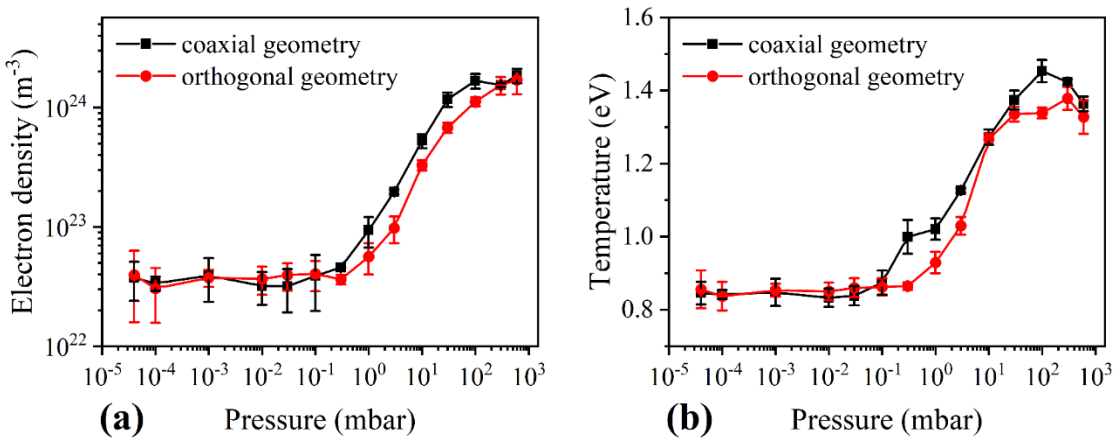

Fig. 6 Pressure dependence of (a) electron density and (b) electron temperature of laser-ablated Mo plasma measured in coaxial and orthogonal detection geometries.

Based on the above analysis, the wavelength shifts measured in the coaxial and orthogonal geometries can be written as:

$$\Delta\lambda_{\parallel}(p) = \Delta\lambda_{D,\parallel}(p) + \Delta\lambda_{Stark,\parallel}(p) \quad (3)$$

$$\Delta\lambda_{\perp}(p) = \Delta\lambda_{D,\perp}(p) + \Delta\lambda_{Stark,\perp}(p) \quad (4)$$

Because the Doppler contribution in the orthogonal geometry is strongly suppressed, $\Delta\lambda_{D,\perp}(p)$ is much smaller than $\Delta\lambda_{D,\parallel}(p)$. Therefore, subtracting the peak wavelength measured in the orthogonal geometry from that measured in the coaxial geometry can largely reduce the common Stark-shift contribution while primarily retaining the Doppler-shift contribution:

$$\Delta\lambda_{\parallel}(p) - \Delta\lambda_{\perp}(p) \approx \Delta\lambda_{D,\parallel}(p) + \Delta\lambda_{Stark,res}(p) \quad (5)$$

$$\Delta\lambda_{Stark,res}(p) = \Delta\lambda_{Stark,\parallel}(p) - \Delta\lambda_{Stark,\perp}(p) \quad (6)$$

When the pressure is below 10 mbar, $\Delta\lambda_{Stark,res}(p)$ is expected to be small because n_e and T_e obtained from the two geometries are similar. Thus, the differential wavelength shift mainly reflects the Doppler shift associated with the axial expansion velocity of the Mo plasma. In the pressure range of 10-10^2 mbar, however, the difference in n_e between the two geometries becomes more pronounced. At 10^2 mbar, the n_e values obtained in the coaxial and orthogonal geometries are 1.67×10^{24} and 1.12×10^{24} m^{-3}, respectively, corresponding to the maximum density difference of 5.5×10^{23} m^{-3}. Based on the correlation between the wavelength shift measured in the orthogonal geometry and n_e, as inferred from Figs. 5 and 6, the resulting residual Stark shift, $\Delta\lambda_{Stark,res}$, is roughly estimated to be 0.003 nm at this pressure. Therefore, the differential method can effectively suppress, but not completely eliminate, the influence of the Stark shift. Overall, the pressure-dependent peak wavelength of the Mo I 428.8631 nm line shows a clear dependence on the detection geometry. In the coaxial geometry, the peak wavelength varies significantly with pressure because the measured Doppler shift is sensitive to changes in the axial plume velocity. In contrast, the Doppler contribution is strongly suppressed in the orthogonal geometry, resulting in a much weaker pressure dependence of the peak wavelength. The similar pressure-dependent trends of n_e and T_e obtained in the two geometries at pressures below 10 mbar further support the use of the orthogonal measurement as a reference for reducing the common Stark contribution. Consequently, the differential wavelength shift between the coaxial and orthogonal geometries provides an effective means of extracting the Doppler-related contribution and characterizing the pressure-dependent axial expansion dynamics of the Mo plasma. Nevertheless, in the transition-pressure regime of 10-10^2 mbar, geometry-dependent differences in n_e introduce a residual Stark contribution, indicating that the differential method suppresses rather than completely eliminates Stark-shift effects.

Pressure-dependent expansion velocities of Mo atoms and ions. Based on the above analysis, because the Doppler shift is significantly affected by the detection geometry, the Doppler effect can be used to infer the plasma expansion velocity along the target surface normal. For a source moving toward the observer, the wavefronts are compressed along the direction of motion, resulting in an increased observed frequency and a decreased observed wavelength. The relationship can be written as:

$$v = \frac{c \cdot \Delta\lambda_D}{\lambda_0} \quad (7)$$

Where λ_0 is the original wavelength obtained from the Kurucz database[34], and $\Delta\lambda_D$ is the Doppler-induced wavelength shift. Based on the above analysis, the Doppler contribution is significant in the coaxial geometry but is largely suppressed in the

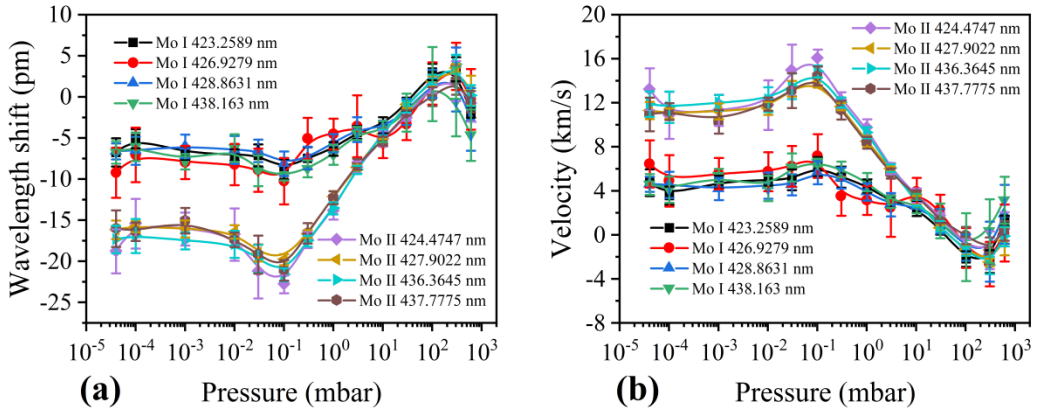

Fig. 7 Pressure dependence of (a) the differential wavelength shifts of Mo atomic and ionic spectral lines and (b) the corresponding velocities inferred from the peak shifts.

orthogonal geometry. Because the electron density and electron temperature obtained in the two geometries are generally comparable under the same pressure, the Stark shift can be regarded as an approximately common-mode contribution to the measured peak wavelength shift, especially in the low-pressure regime. Therefore, the Doppler-induced wavelength shift in the coaxial geometry can be estimated by subtracting the peak wavelength measured in the orthogonal geometry from that measured in the coaxial geometry:

$$\Delta\lambda_D \approx \lambda_{\parallel} - \lambda_{\perp} \tag{8}$$

Where $\lambda_{\parallel}$ and $\lambda_{\perp}$ are the peak wavelengths measured in the coaxial and orthogonal detection geometries, respectively. The expansion velocity along the target surface normal can then be inferred from Eq. (7). It should be noted that at higher pressures, where the electron densities obtained in the two geometries show certain deviations, residual Stark shifts may remain and introduce additional uncertainty into the derived velocity.

Figure. 7(a) shows the Doppler-related differential wavelength shifts of several Mo I and Mo II spectral lines at different ambient pressures (4×10^{-5}-6×10^{2} mbar). The Doppler wavelength shift was obtained by subtracting the peak wavelength measured in the orthogonal geometry from that measured in the coaxial geometry. Overall, the shifts of different lines exhibit highly consistent pressure-dependent trends, indicating systematic behavior governed by plume dynamics and plume-gas interactions. In the low-pressure regime (4×10^{-5}-3×10^{-2} mbar), most lines show a small, weakly varying blueshift, forming a relatively flat plateau. Around 10^{-1} mbar, the wavelength shift exhibits a clear "valley", implying that plume-gas coupling begins to significantly modify the velocity field and the spatial distribution of the emitting region. In the higher-pressure regime (≥1 mbar), the wavelength shift increases rapidly from negative values toward approximately zero. This behavior indicates that, with increasing pressure, enhanced collisions and intensified momentum dissipation markedly reduce the effective line-of-sight velocity projection in the coaxial geometry, thereby weakening the Doppler contribution. Moreover, Mo II lines exhibit systematically larger shift magnitudes than Mo I lines at low pressures (<1 mbar), whereas the disparity progressively diminishes at higher pressures (>10 mbar).

Figure 7(b) presents the plasma expansion velocities along the target surface normal inferred from the wavelength shifts in Fig. 7(a) using Eq. (7), with the positive direction defined toward the observer. Because the velocity is derived directly from the Doppler-related wavelength shift, the pressure-dependent evolution in Fig. 7(b) closely follows that in Fig. 7(a), as expected from the classical Doppler relation. Specifically, a larger blueshift magnitude corresponds to a higher expansion velocity toward the observer, whereas a wavelength shift approaching zero corresponds to a reduction in the line-of-sight velocity. At 4×10^{-5}-3×10^{-2} mbar, both atomic and ionic velocities are relatively high and remain nearly pressure-independent, indicating nearly free expansion in this pressure range. Mo ions reach velocities of approximately 11-15 km/s, whereas Mo atoms reach about 4-6 km/s. This difference can be attributed to acceleration by a transient plasma sheath. The electric field established across the sheath preferentially accelerates ions along the plume expansion direction. Near 10^{-1} mbar, the velocities derived from the spectral lines exhibit a maximum, corresponding to the "valley" in Fig. 7(a). This increase in the measured velocity is more appropriately interpreted as an apparent acceleration caused by redistribution of the emission weighting, rather than as a real acceleration of the entire plasma plume by the background gas. The background gas is not yet sufficient to significantly decelerate the fast particles, but it can already enhance the radiative contribution from the plume front or the fast component through collisional excitation at 10^{-1} mbar[40]. This indicates that, within this pressure range, the spectral signal may no longer originate predominantly from the bulk

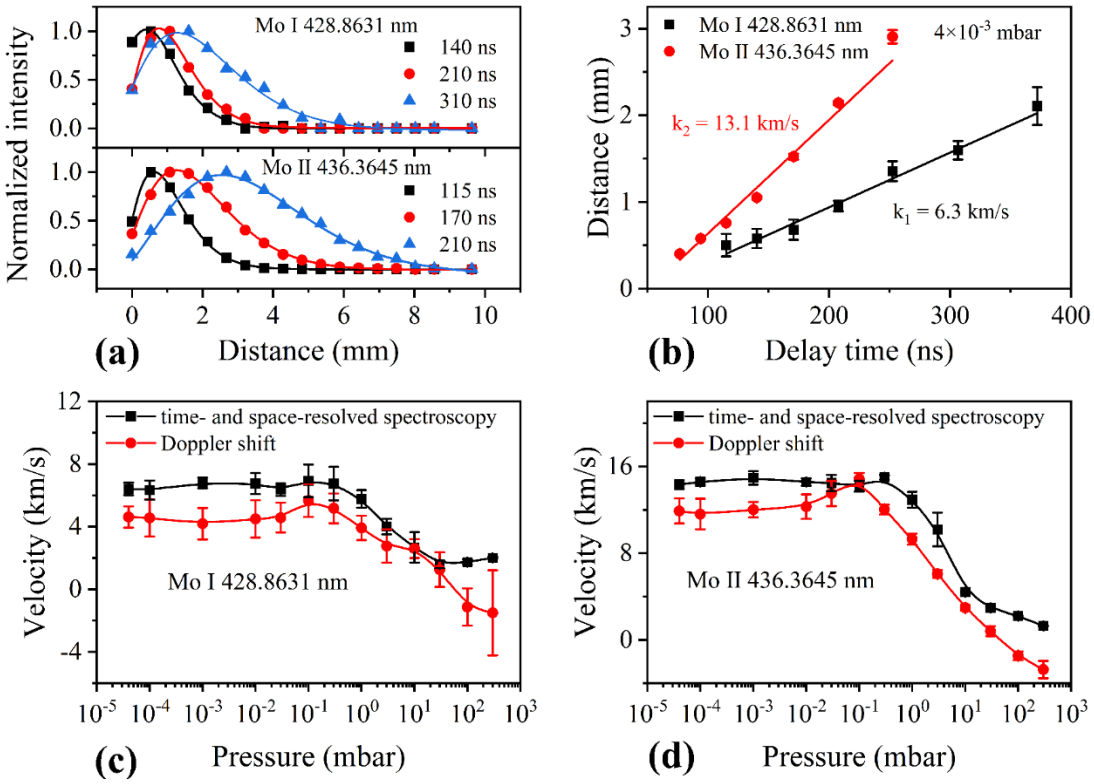

Fig. 8 (a) Spatial distributions of the normalized intensities of Mo I 428.8631 nm and Mo II 436.3645nm at different delay times; (b) temporal evolution of the position of the intensity peak; pressure dependence of the expansion velocities of (c) Mo I 428.8631 nm and (d) Mo II 436.3645 nm obtained by the Doppler shift and time- and space-resolved spectroscopy.

plasma observed under vacuum conditions, but rather from fast emitting species located near the plume front. For pressures above 1 mbar, the velocities decrease sharply with increasing pressure, implying strong background gas confinement and a rapid decay of the expansion velocity.

Figure 8(a) shows the spatial evolution of the normalized intensities of Mo I 428.8631 nm and Mo II 436.3645 nm along the target surface normal at different delay times at 4×10^{-5} mbar. The experimental setup for the time- and space-resolved LIBS measurements has been reported in our previous work[39]. With increasing delay time, the position of the intensity peak shifts away from the target surface, indicating continuous outward expansion of the plasma plume in vacuum. To quantify the position of the intensity peak at each delay time, the intensities of spectral line-distance profiles were fitted, yielding the peak distance $d_{peak}(t)$ along the surface normal. Fig. 8(b) plots the fitted $d_{peak}(t)$ as a function of delay time t. A linear fit to this relationship was then performed, and its slope represents the characteristic expansion velocity of the plasma along the surface normal. Under the present vacuum condition, the inferred normal expansion velocities are 6.3 km/s for Mo I 428.8631 nm and 13.1 km/s for Mo II 436.3645 nm.

By applying the same procedure, the expansion velocities of Mo atoms (Mo I 428.8631 nm) and Mo ions (Mo II 436.3645 nm) at different ambient pressures were further determined, as shown in Fig. 8(c, d). It should be noted that different time intervals were selected at different pressures because the plume expansion dynamics, emission lifetime, and signal-to-noise ratio vary significantly with ambient pressure. Specifically, in the pressure range of 4×10^{-5}-1 mbar, the time interval of 115-370 ns was used for Mo atoms, whereas 75-250 ns was selected for Mo ions. At higher pressures of 30-3×10^{2} mbar, the time interval was extended to 210-1180 ns for Mo atoms and 75-1180 ns for Mo ions, owing to the slower plume expansion and longer emission duration under stronger plume-background gas interactions. In the transition-pressure regime, where the twin-peak distribution appears[27], the delay time interval was selected to ensure that the two peaks could be clearly resolved.

Good agreement is observed between the Doppler-shift method and time- and space-resolved spectroscopy in the overall pressure-dependent evolution of the normal expansion velocities. At 4×10^{-5}-3×10^{-2} mbar, high and relatively stable expansion velocities are obtained by both methods, and the ionic (Mo II) velocity is significantly higher than the atomic (Mo I) velocity. At pressures exceeding 1 mbar, both diagnostics reveal a pronounced velocity reduction, consistent with enhanced collisions and confinement by

the background gas. Similar pressure-dependent behavior has been reported by Harilal et al.[27], who investigated laser-ablated Al plasma over several orders of magnitude in ambient pressure using fast imaging and time-resolved emission spectroscopy. They observed higher velocities for ionized species than for neutral species in the free-expansion regime and a transition from free expansion to plume splitting and subsequently to collision-dominated deceleration with increasing pressure. These similarities provide broader support for the pressure-dependent plume dynamics observed in the present Mo plasma.

Despite the consistent overall trends, systematic quantitative differences are observed between the two methods. In the low-pressure regime, the Doppler-shift method yields Mo II velocities of approximately 11-15 km/s, compared with 14-15 km/s obtained by time- and space-resolved spectroscopy, while the corresponding Mo I velocities are approximately 4-6 and 6-7 km/s, respectively. These differences can be attributed to the distinct diagnostic principles of the two approaches. The Doppler-shift method measures the line-of-sight velocity component of the emitting species and provides an emission-weighted average over the collected emission volume. In contrast, the time- and space-resolved spectroscopy method determines the apparent propagation velocity of the emission maximum, which is influenced not only by particle motion but also by the spatial distribution of excitation, emission lifetime, and signal intensity. Therefore, the two methods provide complementary but not strictly identical velocity information. Overall, despite these differences, the two independent diagnostic approaches provide mutually corroborating evidence for the expansion dynamics of the plasma plume across a broad pressure range. The combined results reveal three characteristic pressure regimes: nearly free expansion at low pressures, an apparent velocity maximum near 10^{-1} mbar associated with redistribution of the emitting population, and strong collisional deceleration above 1 mbar.

Beyond the pressure-dependent velocity trends, the present results provide several methodological and physical insights into laser-ablated plasma diagnostics. First, the comparison between coaxial and orthogonal detection geometries shows that the measured spectral peak position is strongly geometry dependent because of the different line-of-sight velocity components, indicating that detection geometry should be carefully considered when Doppler shifts are interpreted in expanding plasmas. Second, the differential use of the two geometries provides a practical means of suppressing the common Stark-shift contribution and extracting the Doppler-related component. Although residual Stark effects remain in the transition-pressure regime, their magnitude was approximately evaluated from the geometry-dependent electron-density difference, indicating that the residual contribution is limited and can be assessed quantitatively. Third, the pressure-dependent behaviors of Mo atoms and ions provide a species-resolved characterization of the evolution from nearly free expansion to collision-dominated plume dynamics. These observations demonstrate that the differential Doppler-shift method can provide information complementary to plume-front or emission-maximum measurements by directly probing the velocity of specific emitting species.

CONCLUSIONS

This study investigated the expansion dynamics of nanosecond laser-ablated Mo plasma at different ambient pressures (4×10^{-5}-6×10^{2} mbar). By combining optical emission spectroscopy measurements acquired in coaxial and orthogonal detection geometries with Voigt fitting, a non-contact velocity inference method based on Doppler effect was established. The Doppler contribution is significant in the coaxial geometry but strongly suppressed in the orthogonal geometry, while the Stark-shift contribution behaves approximately as a common-mode term between the two geometries, particularly in the low-pressure regime. Therefore, the dominant Doppler-related contribution can be estimated from the difference between the peak wavelengths measured in the two geometries, allowing the characteristic expansion velocity along the target surface normal to be inferred.

The results show a pronounced geometry-dependent effect in the pressure dependence of the peak wavelength. The coaxial geometry is more sensitive to pressure because of the significant Doppler contribution, whereas the orthogonal geometry suppresses this contribution. The similar n_e and T_e values obtained in the two geometries over most of the investigated pressure range indicate comparable Stark-shift contributions, supporting the use of the differential method. However, at 10-10^2 mbar, the increased difference in n_e may introduce a residual Stark shift. At 10^2 mbar, this residual Stark shift was approximately estimated to be 0.003 nm based on the electron density difference between the two detection geometries.

In terms of the pressure dependence of velocity, both Mo atoms and ions exhibit clear regime-dependent behavior. At low pressures of 4×10^{-5}-3×10^{-2} mbar, the plume expands nearly freely, with Mo I velocities of about 4-6 km/s and Mo II velocities of about 11-15 km/s. The higher ionic velocity is attributed to acceleration by the transient plasma sheath. Around 10^{-1} mbar, apparent local maxima in the inferred velocities of both species are observed, which are attributed to a redistribution of the emission weighting rather than to a real acceleration of the entire plasma plume. Above 1 mbar, enhanced collisions and confinement by the background gas cause the expansion velocity to decrease rapidly with pressure. In addition, a comparison of the velocities inferred from the Doppler shift and those obtained from the time- and space-resolved spectroscopy shows good agreement in the pressure-dependent trend. The differences between the velocities

obtained by the two methods can be attributed to their different diagnostic principles: the Doppler-shift method reflects the emission-weighted line-of-sight velocity of emitting species, whereas the time- and space-resolved spectroscopy method gives the apparent propagation velocity of the emission maximum.

Overall, this work elucidates how ambient pressure and detection geometry govern the peak-wavelength shift and expansion dynamics of laser-ablated Mo plasma. The methodological novelty of the present study lies in the differential use of coaxial and orthogonal detection geometries to suppress common spectral-shift contributions and obtain species-resolved Doppler velocities. Unlike plume-front or emission-maximum measurements, this approach directly probes the line-of-sight velocity of individual emitting species and therefore provides complementary information on plasma expansion dynamics. These results provide an experimental basis for improving the interpretation and comparability of LIBS measurements over a wide pressure range and support in situ wall-material and impurity diagnostics for devices such as EAST.

Future work will focus on extending the present differential Doppler-shift approach to multiple observation angles. Doppler shifts measured at different angles can provide the corresponding line-of-sight velocity components, which may be combined to reconstruct the expansion velocity field and further characterize the angular anisotropy of laser-ablated Mo plasma. Time-resolved Doppler measurements with shorter detection gates could also reveal the temporal evolution of the velocity distribution. Combining multi-angle and time-resolved Doppler spectroscopy with time- and space-resolved diagnostics may ultimately provide a more complete description of species-resolved plume dynamics.

AUTHOR INFORMATION

Ding Wu received his BSc and PhD from Dalian University of Technology. He is an associate professor in School of Physics at Dalian University of Technology. He has conducted visiting research at Lawrence Berkeley National Laboratory, Forschungszentrum Jülich, and the Dalian Institute of Chemical Physics, Chinese Academy of Sciences. His work covers plasma–wall material interaction, LIBS and mass spectrometry diagnostics, numerical simulation of laser ablation plasmas, and development of laser Thomson scattering spectrometric instrumentation. He has published over 60 papers and holds 4 authorized national invention patents.

Hongbin Ding received his PhD with the highest honors from the University of Basel, Switzerland, under the supervision of Academician J. P. Maier, and was awarded the Josef Pliva Award for international high-resolution molecular spectroscopy. He is a Second-Class Professor at

Dalian University of Technology, Director of the Academic Committee of the School of Physics, and Director of the Sino-Russian-Belarusian Joint Research Center for Plasma. His work focuses on advanced laser spectroscopic diagnostic techniques and their applications to nuclear fusion plasma–wall interaction, in-situ LIBS diagnostics, high-resolution molecular spectroscopy, and development of laser Thomson scattering spectrometric instrumentation. He has published over 200 papers and holds more than 20 authorized national invention patents.

Corresponding author

* D. Wu

Email address: dingwu@dlut.edu.cn

* H. B. Ding

Email address: hding@dlut.edu.cn

Notes

The authors declare no competing financial interest.

ACKNOWLEDGMENTS

This research was supported by the National MCF Energy R&D Program of China (2022YFE03200100, 2024YFE03000202), the National Natural Science Foundation of China (12005034)

REFERENCES

1. Federici, G., Skinner, C. H., Brooks, J. N., Coad, J. P., Grisolia, C., Haasz, A. A., Hassanein, A., Philipps, V., Pitcher, C. S., Roth, J., Wampler, W. R., and Whyte, D. G. *Nucl. Fusion*, 2001, **41**, 1967-2137. https://doi.org/10.1088/0029-5515/41/12/218
2. Pitts, R. A., Coad, J. P., Coster, D. P., Federici, G., Fundamenski, W., Horacek, J., Krieger, K., Kukushkin, A., Likonen, J., Matthews, G. F., Rubel, M., Strachan, J. D., and JET-EFDA Contributors. *Plasma Phys. Control. Fusion*, 2005, **47**, B303-B322. https://doi.org/10.1088/0741-3335/47/12B/S22
3. Parker, R., Janeschitz, G., Pacher, H. D., Post, D., Chiocchio, S., Federici, G., and Ladd, P. *J. Nucl. Mater.*, 1997, **241-243**, 1-26. https://doi.org/10.1016/S0022-3115(97)80027-X
4. Skinner, C. H., and others. *J. Nucl. Mater.*, 1997, **241-243**, 214-226. https://doi.org/10.1016/S0022-3115(97)80041-4
5. Duan, C., Liu, Y.-L., Zhou, H.-B., Zhang, Y., Jin, S., Lu, G.-H., and Luo, G. N. *J. Nucl. Mater.*, 2010, **404**, 109-115. https://doi.org/10.1016/j.jnucmat.2010.06.029
6. Xuan, C., Zhu, D., Li, C., Guo, Z., Gao, B., Ding, R., Wang, B., Yu, B., Lei, Y., Chen, J., and the EAST Team. *Nucl. Mater. Energy*, 2023, **34**, 101377. https://doi.org/10.1016/j.nme.2023.101377
7. Shen, Y.-C., Lyu, B., Wang, F.-D., Shi, Y.-J., Wu, B., Li, Y.-Y., Fu, J., Wan, B.-N., and the EAST Team. *Chin. Phys. Lett.*, 2016, **33**, 065205. https://doi.org/10.1088/0256-307X/33/6/065205

8. Wan, B. N., Liang, Y., Gong, X. Z., Xiang, N., Xu, G. S., Sun, Y., Wang, L., Qian, J. P., Liu, H. Q., Zeng, L., Zhang, L., Zhang, X. J., Ding, B. J., Zang, Q., Lyu, B., Garofalo, A. M., Ekedahl, A., Li, M. H., Ding, F., Ding, S. Y., Du, H. F., Kong, D. F., Yu, Y., Yang, Y., Luo, Z. P., Huang, J., Zhang, T., Zhang, Y., Li, G. Q., Xia, T. Y., the EAST Team, and Collaborators. *Nucl. Fusion*, 2019, **59**, 112003. https://doi.org/10.1088/1741-4326/ab0396
9. Liu, Z. X., Gao, X., Liu, S. C., Ding, S. Y., Xia, T. Y., Zhang, T., Zhang, S. B., Wang, Y. M., Han, X., Li, J. G., Yang, Y., Jie, Y. X., Ling, B. L., and the EAST Team. *Nucl. Fusion*, 2013, **53**, 073041. https://doi.org/10.1088/0029-5515/53/7/073041
10. Pan, C. *Nucl. Fusion*, 2024, **64**, 076047. https://doi.org/10.1088/1741-4326/ad5218
11. Yan, R., Peng, J., Li, C., Xu, G., Ding, R., Zheng, W., Gao, B., Zhu, D., Wang, B., Mu, L., Chen, J., Gou, F., You, Y., Ye, Z., Zhang, K., and Si, X. *Nucl. Mater. Energy*, 2022, **30**, 101103. https://doi.org/10.1016/j.nme.2021.101103
12. Soni, S., Atikukke, S., Veis, M., Bolouki, N., Ďurina, P., Dvořák, P., Mrkvičková, M., Grigore, E., and Veis, P. *Spectrochim. Acta B*, 2024, **216**, 106930. https://doi.org/10.1016/j.sab.2024.106930
13. Miškovičová, J., Anguš, M., van der Meiden, H., and Veis, P. *Fusion Eng. Des.*, 2020, **153**, 111488. https://doi.org/10.1016/j.fusengdes.2020.111488
14. Liu, J., Wu, D., Fu, C., Hai, R., Yu, X., Sun, L., and Ding, H. *Plasma Sci. Technol.*, 2019, **21**, 034017. https://doi.org/10.1088/2058-6272/aaf821
15. Maurya, G. S., Marín-Roldán, A., Veis, P., Pathak, A. K., and Sen, P. *J. Nucl. Mater.*, 2020, **541**, 152417. https://doi.org/10.1016/j.jnucmat.2020.152417
16. van der Meiden, H. J., Almaviva, S., Butikova, J., Dwivedi, V., Gasior, P., Gromelski, W., Hakola, A., Jiang, X., Jõgi, I., Karhunen, J., Kubkowska, M., Laan, M., Maddaluno, G., Marín-Roldán, A., Paris, P., Piip, K., Pisarčík, M., Sergienko, G., Veis, M., Veis, P., Brezinsek, S., and the EUROfusion WP PFC Team. *Nucl. Fusion*, 2021, **61**, 125001. https://doi.org/10.1088/1741-4326/ac31d6
17. Hu, Z., Bai, X., Wu, H., Hai, R., Ding, F., Imran, M., Li, C., Ding, H., and Luo, G. N. *Nucl. Mater. Energy*, 2024, **41**, 101785. https://doi.org/10.1016/j.nme.2024.101785
18. Likonen, J., Almaviva, S., Rayaprolu, R., Yi, R., Jepu, I., Sergienko, G., Widdowson, A., Jones, N., Atikukke, S., Dittmar, T., Karhunen, J., Gasior, P., Kawan, C., Sackers, M., Soni, S., Wüst, E., Brezinsek, S., Butikova, J., Gromelski, W., Hakola, A., Jõgi, I., Paris, P., Ristkok, J., Veis, P., and the UKAEA RACE Team. *Nucl. Mater. Energy*, 2025, **45**, 102021. https://doi.org/10.1016/j.nme.2025.102021
19. Mazhir, S. N. *ARPN J. Eng. Appl. Sci.*, 2018, **13**, 864-869.
20. Mazhir, S. N., Abdullah, N. A., Rauuf, A. F., and al-Ahmed, H. I. *Baghdad Sci. J.*, 2018, **15**, 81-86. https://doi.org/10.21123/bsj.2018.15.1.0081
21. Soumyashree, S., and Kumar, P. *Spectrochim. Acta B*, 2023, **208**, 106761. https://doi.org/10.1016/j.sab.2023.106761
22. Jõgi, I., Ristkok, J., Butikova, J., Raud, J., and Paris, P. *Nucl. Mater. Energy*, 2023, **37**, 101543. https://doi.org/10.1016/j.nme.2023.101543
23. Farid, N., Harilal, S. S., Ding, H., and Hassanein, A. *J. Appl. Phys.*, 2014, **115**, 033107. https://doi.org/10.1063/1.4862167
24. Wang, J., Hu, J., Yu, Y., and Cao, B. *Vacuum*, 2021, **183**, 109854. https://doi.org/10.1016/j.vacuum.2020.109854
25. Gao, X., Hu, J. S., Zhao, Y. P., Gong, X. Z., Yu, Y. W., Luo, G. N., Guo, H. Y., Morita, S., Hu, L. Q., Chen, J. L., Wang, H. Y., Wang, X. M., Zhang, X. D., Li, J. G., and the EAST Team. *J. Nucl. Mater.*, 2009, **390-391**, 864-868. https://doi.org/10.1016/j.jnucmat.2009.01.226
26. Hu, J. S., Wang, X. M., Li, J. H., Wu, J. H., Chen, Y., Wang, H. Y., Yang, D. W., Luo, N. C., Li, S. F., Li, G. Y., Wang, L., Yu, Y. W., Dou, R. C., Hu, Q. S., Bao, L. M., Zhao, Y. P., Li, J. G., and the EAST Vacuum and Wall Conditioning Group. *Fusion Eng. Des.*, 2009, **84**, 2167-2173. https://doi.org/10.1016/j.fusengdes.2009.03.016
27. Harilal, S. S., Bindhu, C. V., Tillack, M. S., Najmabadi, F., and Gaeris, A. C. *J. Appl. Phys.*, 2003, **93**, 2380-2388. https://doi.org/10.1063/1.1544070
28. Zhang, S., Wang, X., He, M., Jiang, Y., Zhang, B., Hang, W., and Huang, B. *Spectrochim. Acta B*, 2014, **97**, 13-33. https://doi.org/10.1016/j.sab.2014.04.009
29. Cristoforetti, G., Legnaioli, S., Palleschi, V., Salvetti, A., and Tognoni, E. *Spectrochim. Acta B*, 2004, **59**, 1907-1917. https://doi.org/10.1016/j.sab.2004.09.003
30. Whitty, W., and Mosnier, J. P. *Appl. Surf. Sci.*, 1998, **127-129**, 1035-1040. https://doi.org/10.1016/S0169-4332(97)00603-X
31. Camacho, J. J., Díaz, L., Santos, M., Juan, L. J., and Poyato, J. M. L. *J. Appl. Phys.*, 2010, **107**, 083306. https://doi.org/10.1063/1.3382914
32. Irimiciuc, S., Bulai, G., Agop, M., and Gurlui, S. *Appl. Phys. A*, 2018, **124**, 615. https://doi.org/10.1007/s00339-018-2035-1
33. Dawood, M. S., Hamdan, A., and Margot, J. *AIP Adv.*, 2015, **5**, 107143. https://doi.org/10.1063/1.4935100
34. Smith, P. L., Heise, C., Esmond, J. R., and Kurucz, R. L. Atomic Spectral Line Database from CD-ROM 23 of R. L. Kurucz. Smithsonian Astrophysical Observatory, Cambridge, MA, 1995.
35. Konjević, N. *Phys. Rep.*, 1999, **316**, 339-401. https://doi.org/10.1016/S0370-1573(98)00132-X
36. Einstein, A. *Ann. Phys.*, 1905, **17**, 891-921. https://doi.org/10.1002/andp.19053221004
37. Li, C., Wang, J., and Wang, X. *Phys. Lett. A*, 2014, **378**, 3319-3325. https://doi.org/10.1016/j.physleta.2014.06.049
38. Palya, A., Ranjbar, O. A., Lin, Z., and Volkov, A. N. *Int. J. Heat Mass Transf.*, 2019, **132**, 1029-1052. https://doi.org/10.1016/j.ijheatmasstransfer.2018.12.002
39. Hu, X., Wu, H., Wu, D., Wang, X., Liu, S., Xu, K., Hai, R., Li, C., Feng, C., and Ding, H. *J. Anal. At. Spectrom.*, 2025, **40**, 2362-2372. https://doi.org/10.1039/D5JA00157A
40. Amoruso, S., Sambri, A., and Wang, X. *J. Appl. Phys.*, 2006, **100**, 013302. https://doi.org/10.1063/1.2207500